Modified breathing mechanism model and phase waterfall plot diagnostic method for cracked rotors[†]

Jingsong Xie, Wei Cheng[*] and Yanyang Zi

State Key Laboratory for Manufacturing Systems Engineering, Xi'an Jiaotong University, 710049, China

---

Abstract

Transverse breathing cracks are a primary damage mode in rotor systems and seriously influence the safety and reliability of equipment operation. The vibration characteristics exhibited by cracked rotors when passing through critical speeds serve as important evidence in the diagnosis of cracks, and a breathing mechanism model without weight dominance is needed to study these resonant characteristics. In this work, a restoring force modified model is proposed for studying the breathing mechanism of cracked Jeffcott rotors without weight dominance. Furthermore, a novel phase waterfall plot method that can identify frequency components with weak amplitudes is proposed to analyze the vibration response characteristics of cracked Jeffcott rotors. Numerical and experimental studies indicate that the phase waterfall plots effectively recognize the weak characteristic frequencies of cracked rotors. This study can also provide references for the crack monitoring of rotor systems.

Keywords: Breathing mechanism model; Cracked Jeffcott rotors; Phase waterfall plot; Weak characteristic frequency

---

1. Introduction

Rotor-disc systems are widely applied in such fields as power supply systems, aeronautics, astronautics, and navy equipment. However, material defects, manufacturing flaws, and cyclic loadings usually cause cracks in the rotating components of these systems. Transverse cracks are common in rotors and seriously influence the safety and reliability of equipment operation. The vibration characteristics of cracked rotors traversing critical speeds are important references in the fault diagnosis of cracks. Therefore, these resonant characteristics must be studied.

The first step to studying the resonant characteristics exhibited by rotors passing through critical speeds is constructing a model without the weight dominance of a breathing crack in the damaged system. The transverse crack alternately opens and closes (complex "breathing effect") due to gravity and unbalanced forces, thereby resulting in periodically changed stiffnesses. Research on the breathing mechanism aims to determine the stiffness breathing functions of cracked rotors. Mayes [1] proposed a method that studies the stiffnesses of shafts containing cracks that change with shaft depth. Sekhar [2] used a simple hinge model to describe the breathing action of small cracks. Sinou [3, 4] solved the dynamic response of a cracked rotor with a cosine breathing function. Sawicki [5] developed a strategy that can analyze the vibration response of a cracked rotor with and without weight dominance. These studies describe the time-varying stiffness of cracked rotors, but these models do not precisely reveal the breathing mechanism of such rotors. Mohammad [6-8] defined two new breathing functions to represent the actual breathing effect on the cracked element stiffness matrix. Bachschmid [9, 10] modeled the breathing functions of cracks with a numerical method that discretizes a crack section into many area elements. The total closed area of the crack section is also constituted by all the area elements in a compressive stress state. This model can also be used to analyze the breathing mechanism of cracked rotors with weight dominance on the basis of the stress changes of the cross section. However, when a cracked rotor passes through the critical speed, the vibration (whirl) of the rotor becomes excessively complicated and not synchronized with rotation. The dynamic response of the rotor increases rapidly, and the assumption of weight dominance becomes unreliable [11]. Therefore, a breathing mechanism model without weight dominance must be used to study these resonant characteristics.

Aside from breathing mechanism modeling, the dynamic behaviors of cracked rotors have attracted the attention of many researchers. Bachschmid and Sekhar [12-16] studied a crack identification method that is based on vibration responses and applied it to practical engineering. Dong [17]

---

[*]Corresponding author. Tel.: +86 29 82663689 801, Fax.: +86 29 82663689 805
E-mail address: chengw@mail.xjtu.edu.cn
[†]Recommended by Associate Editor Junhong Park

investigated the effects of crack location and depth on the mode shapes and the changes in the eigenfrequencies of a cracked rotor. Spagnol [18] predicted that a high unbalance eccentricity and a 180° placement of the unbalanced mass will result in the disappearance of 2X and/or 3X harmonic components at one-half and one-third of the rotor critical speed. Zhao [19] developed a finite element model of a cracked shaft-disc system to investigate the coupling of lateral, longitudinal, and torsion vibration, which may indicate damage. Chu [20] investigated the dynamic behaviors of a cracked rotor system with oil-film force and provided reasonable references for the safe operation and the crack diagnosis of rotors. Khorrami [21] formulated an analytical model to study the effects of crack characteristics on selected vibrational properties. Liu [22] found that coupled vibration in lateral and torsional components is an effective indicator of cracks in the presence of torsional excitation. These studies provide references for crack diagnosis, but the current diagnosis methods are not precise. Therefore, the vibration response characteristics of cracked rotor systems should be further studied.

Effective signal processing and visualization methods are the key to extracting dynamic response characteristics and identifying rotor cracks, which have been widely studied by scholars. Sekhar [23] compared the detection performances of short-time Fourier transform, continuous wavelet transform, and Hilbert–Huang transform. Chen [24] analyzed the effectiveness of RMS values, kurtosis values, and frequency spectrum diagrams in the judgment of crack length. Yan [25] used the fast Fourier transform method and the EMD technique to derive the amplitude variation of high-order frequencies and indicated the practicality of the EMD-based crack detection method. Kumar [26] proposed an approach to detecting the combined faults of unbalanced and bent rotors for the advanced detection of the features of fault rotor diagnosis. The aforementioned studies provide effective methods for feature extraction and crack identification. However, these methods are based on the time-domain or frequency-domain amplitude characteristics of signals. Therefore, when a crack produces weak vibration energy and thus small characteristic frequency amplitudes, effectively identifying the characteristic frequencies will be difficult. To improve the accuracy of crack identification, signal processing and feature extraction methods that are more powerful and robust than existing techniques need to be developed.

On the basis of this analysis, this work develops a modified model to study the breathing mechanism of cracked rotors without weight dominance. A novel phase waterfall plot diagnostic method that can identify frequency components with weak amplitudes is proposed for analyzing the simulated and experimental signals of cracked rotors passing through critical speeds.

This paper is organized as follows. Sec. 2 presents the development of new functions of horizontal, vertical, and coupling stiffnesses for modeling the breathing effects of cracked rotors without weight dominance. Sec. 3 explains the use of
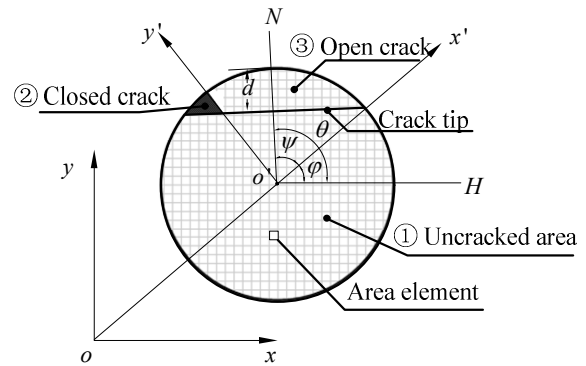

Fig. 1. Diagram of the crack section, fixed coordinate system, and rotating coordinate system.

the new breathing functions to construct the dynamical equations of a cracked rotor; the time-domain waveforms, time–frequency spectrums, and an analysis of the phase waterfall plots of simulated signals when the rotor passes through the critical speed are also included. Sec. 4 discusses the experimental study involving a cracked rotor passing through the critical speed; the effectiveness of the simulation in Sec. 3 is compared and validated. Sec. 5 presents the conclusions.

2. Breathing mechanism

This section explains the proposed restoring force modified model. The restoring force of the cracked rotor in the whirling process can be solved using this method instead of the hypothesis that the direction of the restoring force is parallel to the shaft displacement.

2.1 Algorithm of breathing function

In Fig. 1, *oxy* is a fixed coordinate system, *o'x'y'* is the rotating coordinate system, $\overline{o'N}$ is the normal direction of the crack tip, H is the horizontal reference axis, θ is the rotation angle, φ is the whirling angle, $\psi = \theta - \varphi$ is the rotation–whirling difference angle, and d is the absolute depth of the cracks. The crack depth is defined as $\mu = d / D$, and D is the diameter of the shaft. The crack section comprises three parts, namely, uncracked, open crack, and closed crack areas. The entire section is divided into numerous area elements.

During the rotation of the rotor, the tensile and compression area of the crack section changes with the stress field distribution. This change in area causes the "breathing effect", which is the constant opening and closing of the crack. The centroid and centroid principal inertia axes of the closed area (area ① + ② in Fig. 1) are obtained by considering the influence of the open crack area to the positions of o_I, x_I and y_I, as shown in Fig. 2.

In Fig. 2, $o_I x^* y^*$ is a coordinate system whose origin is at centroid o_I, and whose axis x^* is parallel to the axis x'. x_I and y_I are centroid principal inertia axes. η (η_0) is the angle between the axes x_I and $x^*(x')$. α_i (α_0) is the angle between the
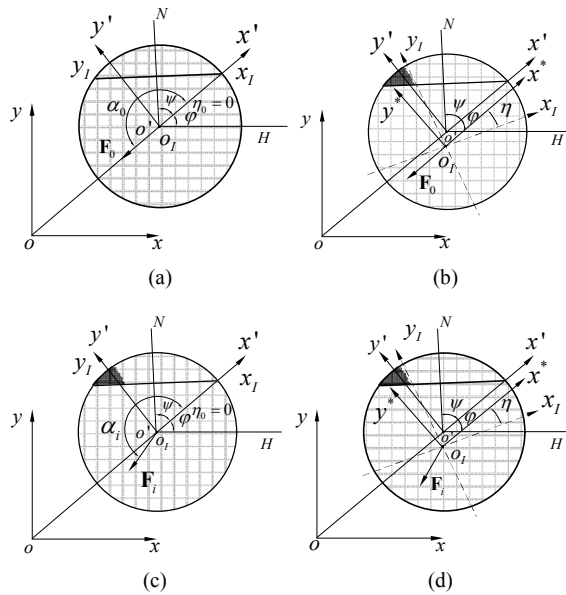
Fig. 2. Iterative processes of the restoring force and the centroid principal inertia axis: (a) Assumptive restoring force and the centroid principal inertia axis; (b) assumptive restoring force and the convergent centroid principal inertia axis; (c) modified restoring force and the assumptive centroid principal inertia axis; (d) modified restoring force and the convergent centroid principal inertia axis.

restoring force F_i and the shaft displacement $\overrightarrow{oo'}$.

The breathing mechanism can be studied by the stress analysis of the cracked cross section during the rotation of the rotor, which can be used to determine the closing area of the crack. The principal inertia moments of the closed area can also be calculated, and the bending stiffness of the local cracked shaft can ultimately be obtained. Bachschmid [11, 12] modeled the breathing function of cracks with a numerical method that discretizes the crack section into numerous area elements. The total closed area of the crack section comprises all the area elements, which are in a compressive stress state. The stress of the crack section is determined by weight or other forces with known directions. Therefore, this model is generally used for heavy rotors. A flowchart of Bachschmid's breathing mechanism model is shown in Fig. 3(a).

For general cracked rotors, the closing and opening of the crack section are not controlled by gravity but by rotation and whirling. To solve the stiffness breathing functions of cracked rotors without weight dominance, the key problem is determining the direction of the restoring force F_i, as shown in Fig. 2. When Bachschmid's model is used in the condition without weight dominance, the direction of the restoring force F_i is assumed to be parallel to the shaft displacement $\overrightarrow{oo'}$. However, the asymmetric stiffnesses of cracked rotors cause the restoring force F_i to be unparallel to the shaft displacement $\overrightarrow{oo'}$, as shown in Fig. 2(c), $F_i \nparallel \overrightarrow{oo'}$ ($\alpha_i \neq -\pi$). A detailed explanation is presented in Sec. 2.4.

In this work, the model in Ref. [11] is modified and a restoring force modified model is developed to study the breath-

ing mechanism of cracked rotors without weight dominance.

The basic process in restoring force modification is that at each rotation–whirling difference angle, the angle of the restoring force is initially assumed and the stress concentration is ignored. Thus, the stress distribution corresponding to the assumed restoring force can be calculated, and the open area and the total closed area can be obtained. Afterward, the stiffness of the equivalent cracked beam (a remarkably short area containing the crack) can be obtained according to the bending theory of beams, as described by Bachschmid [12].

To simplify the model and quantitatively investigate the main mechanical characteristics of Jeffcott rotor models, the z-axis DOF is not considered. Therefore, we consider the open area in the crack section to be throughout the shaft. Then, the breathing stiffness of the cracked Jeffcott rotor can be obtained using the abovementioned method.

This process can greatly simplify the calculations of stiffness and restoring force and can extract the main change law of the breathing stiffness. This simplified model also satisfies the requirements of qualitative vibration characteristic analysis and mechanism explanations of cracked rotors. However, part of the accuracy of the vibration amplitude is lost. All models have limitations, and no absolute best model exists. Therefore, the most appropriate model should be established according to the analysis requirements.

With the combination of the solved stiffness and the current shaft displacement (whirling position) $\overrightarrow{oo'}$, the new restoring force can be calculated. Finally, the angle of the restoring force can be modified by the updated restoring force. In the methods presented above, the stress distribution of the cracked section is no longer determined by gravity but by rotation and whirling, thus overcoming the constraint of weight dominance. A flowchart of the restoring force modified breathing mechanism model is shown in Fig. 3(b).

A comparison of the flowcharts in Figs. 3(a) and (b) shows that the proposed model adds an iterative process for the solution of the restoring force. Instead of the hypothesis that the direction of the restoring force is parallel to the shaft displacement, this method can be used to solve the restoring force of the cracked rotor in the whirling process.

To satisfy the condition without dominance, Bachschmid's model is modified in this study. Details about the processes of the modified model are in the Appendix A.

The breathing stiffness of the cracked Jeffcott rotor system can be solved following the steps in the flowchart and the Appendix A. This section considers four rotors with crack depths of $\mu = 0.05$, $\mu = 0.1$, $\mu = 0.2$ and $\mu = 0.3$.

2.2 Relative stiffness

The relative stiffnesses are shown in Fig. 4. The stiffnesses k_{x*}, k_{y*} and k_{x*y*} change with ψ. In Fig. 4(a), the value of the coupling stiffness k_{x*y*} is close to zero and k_{x*} and k_{y*} are close to K_{max} (K_{max} is the stiffness of the rotor without cracks). Therefore, the breathing effect is not significant at $\mu = 0.05$.
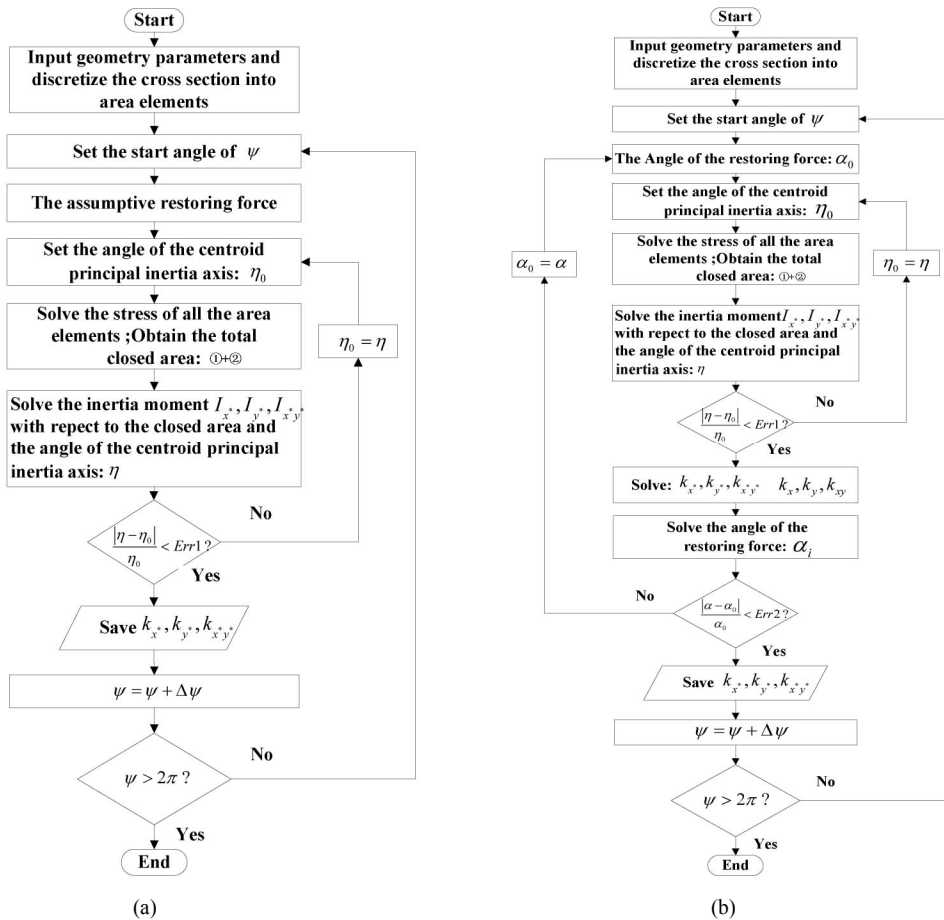
Fig. 3. Flowcharts of the breathing mechanism model: (a) Bachschmid's model; (b) proposed restoring force modified model.
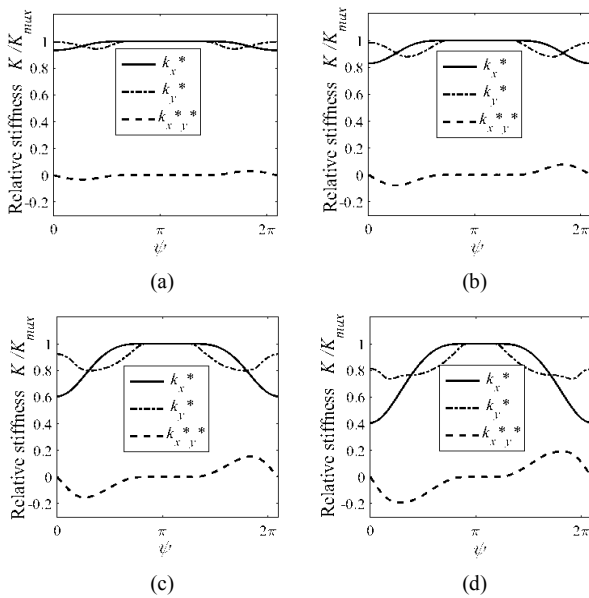

Fig. 4. Relative stiffnesses k_{x*}, k_{y*} and k_{x*y*}: (a) $\mu = 0.05$; (b) $\mu = 0.1$; (c) $\mu = 0.2$; (d) $\mu = 0.3$.

In Figs. 4(a)-(d), the stiffness decreases greatly, which means that the breathing effect becomes increasingly pronounced with the increase in crack depth. The length of the straight part in these four figures decreases with the increase in crack depth, which indicates that the angle range where the crack is fully closed is also decreasing. Therefore, the influence of the crack on the stiffness becomes increasingly remarkable as crack depth increases.

2.3 Discussion

In Sec. 2, the stiffness breathing functions of the cracked rotor are analyzed using the proposed method. However, certain issues still need to be discussed.

When the rotor is cracked, its asymmetric stiffness causes the restoring force $\boldsymbol{F}_i$ to become unparallel to the shaft displacement $\overrightarrow{oo'}$. The restoring force $\boldsymbol{F}_i$ at a certain state is shown in Eq. (A.7). To illustrate the unparallelism of the direction of the restoring force $\boldsymbol{F}_i$ to the shaft displacement $\overrightarrow{oo'}$, Eq. (A.8) is rewritten as follows:

$$\cos\alpha_i = \frac{\boldsymbol{F}_i \overrightarrow{oo'}}{\left|\boldsymbol{F}_i\right|\left|\overrightarrow{oo'}\right|} = \frac{-(k_x x_{o'}^2 + 2k_{xy} y_{o'} x_{o'} + k_y y_{o'}^2)}{\sqrt{\left(x_{o'}^2 + y_{o'}^2\right)\left(\left(k_x x_{o'} + k_{xy} y_{o'}\right)^2 + \left(k_{xy} x_{o'} + k_y y_{o'}\right)^2\right)}} .$$
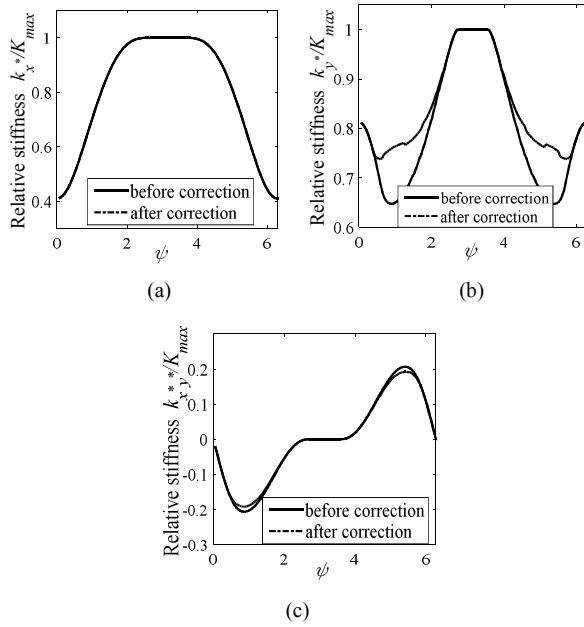
(1)

(a)

(b)

(c)

Fig. 5. Relative stiffnesses before and after modification at $\mu = 0.3$: (a) k_{x*}/K_{max}; (b) k_{y*}/K_{max}; (c) k_{x*y*}/K_{max}.

The stiffnesses of a normal rotor with a circular section are $k_x = k_y = K_{max}$ and $k_{xy} = 0$. In this case, $\cos\alpha_i \equiv -1$, which means that $\mathbf{F}_i$ and $\overline{oo'}$ are in the opposite direction. Therefore, at any position, the directions of restoring force $\mathbf{F}_i$ and shaft displacement are opposite, and the direction of the restoring force $\mathbf{F}_i$ does not need to be modified. However, if the rotor is cracked, then the condition $\cos\alpha_i = -1$ is satisfied only at special whirling positions where the crack is totally closed. Otherwise, the condition $\cos\alpha_i = -1$ cannot be guaranteed because $k_x \neq k_y$ and $k_{xy} \neq 0$. Therefore, the real direction of the restoring force $\mathbf{F}_i$ must be determined according to the iterative calculations proposed in this article.

Accurate stiffness and closed area of the crack can be calculated because the restoring force $\mathbf{F}_i$ can be obtained at any whirling position through the iterative calculations. In Fig. 5, $\mu = 0.3$ is used as an example to show the difference in the stiffnesses before and after the modification of the restoring force. After modification, k_{y*} is greater than before within a certain range, k_{x*y*} shows the reverse trend, and k_{x*} is unchanged. The above results show that the modification reduces the stiffness variation caused by the crack.

Furthermore, modification results match the general principles of mechanics well because the movement is always along the direction of least resistance. Letting $\alpha_i = -\pi$ artificially emphasizes the breathing of the crack, thereby causing the movement to overcome large resistances.

3. Dynamical responses and phase waterfall plot method

3.1 Dynamical equations

In Fig. 6, L is the length of the shaft and z_c is the z-
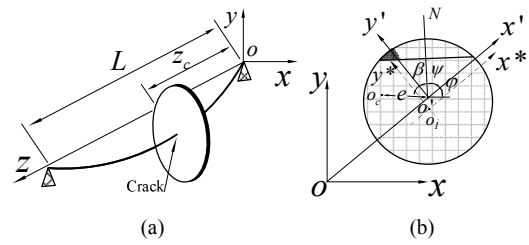

(a)   (b)

Fig. 6. (a) The Jeffcott rotor with the transverse crack; (b) schematic diagram of the cracked cross section.

coordinate of the crack position with respect to the *o-xyz* reference system. o_c is the center of mass, e is the eccentricity, and β is the imbalance orientation angle. The breathing function determines the stiffnesses (k_{x*}, k_{y*}, k_{x*y*}) of the rotor in the rotational coordinate system *o'x'y'*, and the stiffnesses (k_x, k_y, k_{xy}) in the fixed coordinate system *oxy* can be obtained by a transformation of Eq. (A.6). Afterward, the general dynamical equation of the Jeffcott rotor can be established in the fixed coordinate system *oxy* through Eq. (2).

$$M\ddot{u} + C\dot{u} + K(u,t)u = F_s + F_e,\tag{2}$$

where $F_s = \begin{bmatrix} 0 & -mg \end{bmatrix}^T$ is a force caused by the dead weight of the rotor and F_e is an external force caused by the rotation of the rotor.

The external force of the rotor excited by the imbalance when starting with constant acceleration is shown in Eq. (3).

$$F_e = me\begin{bmatrix} \dot{\theta}^2\cos(\theta+\beta) + \ddot{\theta}\sin(\theta+\beta) \\ \dot{\theta}^2\sin(\theta+\beta) - \ddot{\theta}\cos(\theta+\beta) \end{bmatrix},\tag{3}$$

where angular acceleration $\ddot{\theta} = \gamma$ is a constant, $\dot{\theta} = \gamma t + \omega_0$ is the instantaneous angular velocity, $\theta = 0.5\gamma t^2 + \omega_0 t$ is the rotation angle, and ω_0 is the initial angular velocity. Then, the dynamic equations (Eq. (4)) for the starting up can be obtained from Eq. (2).

$$\begin{bmatrix} m & 0 \\ 0 & m \end{bmatrix}\begin{bmatrix} \ddot{x} \\ \ddot{y} \end{bmatrix} + \begin{bmatrix} c & 0 \\ 0 & c \end{bmatrix}\begin{bmatrix} \dot{x} \\ \dot{y} \end{bmatrix} + \begin{bmatrix} k_x(x,y,t) & k_{xy}(x,y,t) \\ k_{xy}(x,y,t) & k_y(x,y,t) \end{bmatrix}\begin{bmatrix} x \\ y \end{bmatrix}$$
$$= me\begin{bmatrix} \dot{\theta}^2\cos(\theta+\beta) + \ddot{\theta}\sin(\theta+\beta) \\ \dot{\theta}^2\sin(\theta+\beta) - \ddot{\theta}\cos(\theta+\beta) \end{bmatrix} - \begin{bmatrix} 0 \\ mg \end{bmatrix}.\tag{4}$$

The parameters selected in the numerical case study are the same as those of the rotor test bed. The parameters of the rotor system are as follows: Length $L = 225$ mm; diameter $D = 10$ mm; mass $m = 2.46$ kg; eccentricity distance $e = D \times 10^{-5}$; damping $c = 2m\omega_c\zeta$, where ω_c is the critical speed; and damping ratio $\zeta = 5 \times 10^{-3}$. Other kinematic parameters are shown in the succeeding simulations. The Runge–Kutta method is used to solve the dynamical equations.
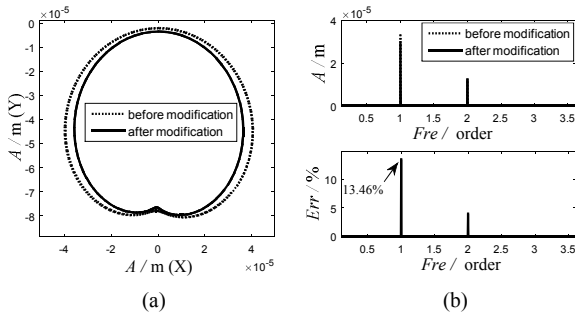
Fig. 7. Dynamic results before and after the restoring force modifications: (a) Axis orbits; (b) frequency spectrums and error rates of harmonic amplitudes.

3.2 Dynamical result comparison

To compare the dynamic results obtained by the restoring force modified model and the previous model, the axis orbits and the frequency spectrums before and after the restoring force modifications are presented in Fig. 7. The kinematic parameters are $\gamma = 0 \text{ rad}/\text{s}^2$ and $\omega_0 = 0.6\omega_c$.

Fig. 7(a) presents the axis orbits before and after the restoring force modifications. Fig. 7(b) shows the frequency spectrums of the displacements and the error rates of the harmonic amplitudes before and after the restoring force modifications. Fig. 7(a) shows that the vibration amplitudes of the X and Y directions are reduced after modification. Fig. 7(b) shows that the amplitudes of the frequency components before and after modification are different; the maximum error rate of the frequency amplitudes is 13.46 %. This result also validates the analysis in Sec. 2.3, which states that before modification, letting $\alpha_i = -\pi$ artificially emphasizes the breathing of the crack, thus causing the vibration amplitudes to become relatively large. The need for model modification is also illustrated.

3.3 Time-domain waveforms

The vibration signals of the cracked rotor passing through the critical speed contain abundant fault characteristic information. Therefore, we mainly study the characteristics of the time-domain waveforms, the amplitude spectrums, and the phase waterfall plots of these vibration signals.

At crack depth $\mu = 0.2$, the dynamic response characteristics of the four cracked rotors with different imbalance orientation angles are solved as the rotor passes through the critical speed. Fig. 8(a) shows the time-domain waveforms of a normal rotor. Figs. 8(b)-(e) show their time-domain waveforms at $\beta = 0, \beta = \pi/2, \beta = \pi$ and $\beta = 3\pi/2$.

Fig. 8(a) shows that at the critical point, only one resonance peak of the normal rotor has a regular shape. In Figs. 8(b)-(e), the time-domain waveforms of the cracked rotors passing through the critical speed are highly related to the imbalance orientation angles.

(1) The resonant amplitudes change with the imbalance orientation angles. The resonant amplitude obtains the maximum
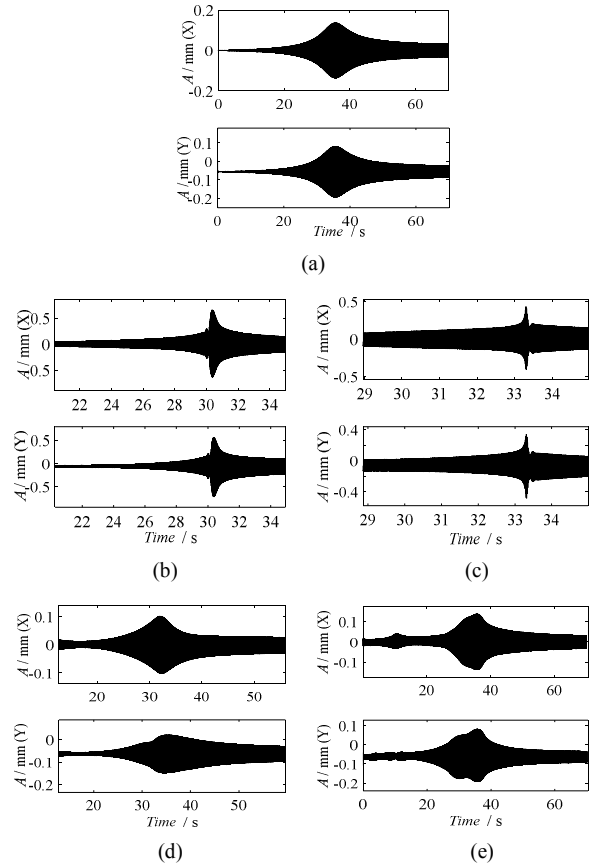

Fig. 8. Time-domain waveforms of cracked rotors passing through the critical speed at $\mu = 0.2$, $\omega_0 = 1000 \text{ r}/\text{min}$ and $\gamma = 9 \text{ rad}/\text{s}^2$: (X) vibration amplitudes in X direction, (Y) vibration amplitudes in Y direction: (a) Normal rotor; (b) $\beta = 0$; (c) $\beta = \pi/2$; (d) $\beta = \pi$; (e) $\beta = 3\pi/2$.

value at $\beta = 0$ (Fig. 8(b)), which is more than 0.5 mm. On the contrary, at $\beta = \pi$ (Fig. 8(d)), the resonant amplitude is less than 0.1 mm, which is the minimum that corresponds to these four phases.

(2) The shapes of the resonance peaks change with the imbalance orientation angles. In Figs. 8(b) and (c), two independent and steep resonance peaks are present, one of which is larger than the other. However, in Figs. 8(d) and (e), the two resonance peaks are coupled together and both are not steep anymore.

These results of the proposed model show that the vibration responses of cracked rotors have different time-domain waveforms for various imbalance orientation angles and double resonance peaks are noticeable features of cracked rotors.

These characteristics are recognized by scholars. The accuracy of the proposed model for major vibration feature extraction is illustrated by the experimental study about the double resonance peaks in Sec. 4.2.

3.4 Phase waterfall plot method

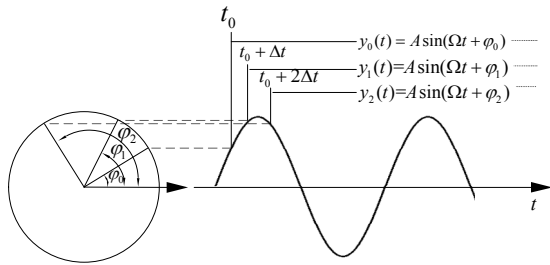A novel phase waterfall plot method is proposed to identify
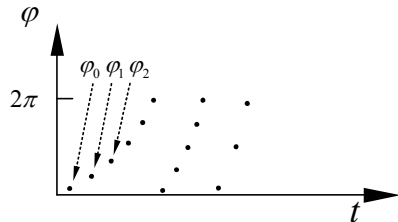
Fig. 9. Diagram of the windowed process.

Fig. 10. Series of initial phases.

Fig. 11. Drawing process of the phase waterfall plot.

the weak frequency components of the cracked Jeffcott rotor.

Cracks in rotors can cause parametric excitation. Therefore, the vibration responses of the cracked system theoretically contain different frequency components other than the rotational frequency (1X) caused by imbalance. However, the energy of the parametric excitation caused by the crack may be excessively small, and finding the characteristic frequencies of the cracks in the amplitude spectrums of the vibration responses is difficult. The amplitude A of a certain frequency component $y(t) = A\sin(\Omega t + \varphi)$ in the vibration responses is associated with the excitation energy, but the initial phase φ is uncorrelated with this energy. Once the frequency component is present, the initial phase will be between $-\pi$ and π. On the basis of this analysis, the phase can be used to identify the weak frequency components, which cannot be identified in amplitude spectrums.

With the vibration response of an acceleration process as an example, the graphing method of the phase waterfall plot is represented as follows.

For an m-point discrete harmonic signal $S = [s_0, s_1, \cdots, s_{m-1}]$, the initial step is making a short-time window move a sampling point every time and multiply with the signal, as shown in Fig. 9. Then, k short-time signals $y_0(t)$, $y_1(t)$, $y_2(t) \cdots y_{k-1}(t)$ can be obtained, where $y_0(t) = [s_0, s_1, \cdots, s_{m-1}]$, $y_1(t)=[s_1, s_2, \cdots, s_n]$, $\cdots$, $y_n(t) = [s_n, s_{n+1}, \cdots, s_{2n-1}]$, and n is the window length $(n \ll m)$. The initial phases $\varphi_0, \varphi_1, \varphi_2, \cdots, \varphi_n$ of these signals are increased, as shown in Fig. 10.

Second, frequency spectrums $Y_0(\omega)$, $Y_1(\omega)$, $Y_2(\omega)$ and $\ldots$, $Y_{k-1}(\omega)$, which correspond to these short-time signals, can be obtained by FFT. The phase spectrums can be calculated by $\Phi_i(\omega) = \arctan\left(I_{Y_i}/R_{Y_i}\right)$, where I_{Y_i} and R_{Y_i} are the imaginary and real parts of $Y_i(\omega)$, respectively. $\Phi_i(\omega)$ are plotted in Fig. 11.

Each single-phase spectrum $\Phi_i(\omega)$ has nonzero values not only at frequency Ω but also at all the other frequencies.
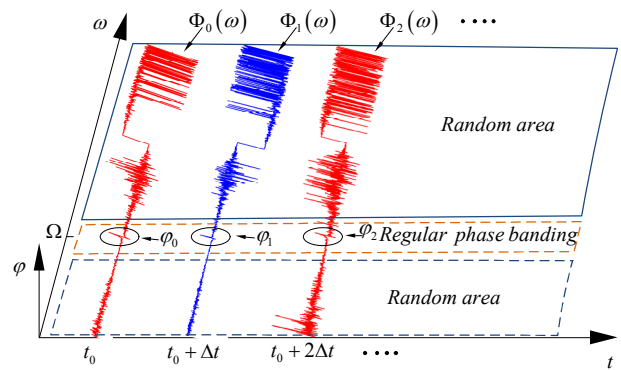
Therefore, we cannot identify the frequency Ω only by each phase's spectrum $\Phi_i(\omega)$ because I_{Y_i} and R_{Y_i} are not zero but random values close to zero at other frequencies. However, if all the phase spectrums $\Phi_i(\omega)$ are arranged in turn, then a phase waterfall plot can be constructed as shown in Fig. 11. As a regular phase banding at frequency Ω is produced, the frequency Ω can be identified.

3.5 Phase waterfall plots and time–frequency amplitude spectrums

The effectiveness and superiority of the phase waterfall plot in recognizing weak characteristic frequencies are verified by the following comparisons.

This section compares the dynamic response characteristics of the vibration displacements of cracked rotors for four imbalance orientation angles $\beta = 0$, $\beta = \pi/2$, $\beta = \pi$ and $\beta = 3\pi/2$ at $\mu = 0.2$ with those of a normal rotor (Figs. 12(a) and (b)).

For the vibration responses in the acceleration process, the phase banding in the phase waterfall plot is oblique. If the vibration responses contain several high-order frequency components, then the phase bandings can form radial lines in the phase waterfall plot, as shown in Figs. 12(d), (f), (h) and (j).

Figs. 12(a) and (b) show that only one frequency component in the amplitude spectrum corresponds to the rotational speed as the rotational speed increases; moreover, the phase waterfall plot shows the same frequency component (without radial lines). Once the crack appears, the characteristics (radial lines) of the phase waterfall plots become noticeable. The radial lines in the phase waterfall plots represent the high-order frequencies of the vibration responses of the cracked rotors. In amplitude spectrum, such amplitudes can hardly be recognized. The detailed characteristics are as follows.

(1) A comparison of the amplitude spectrums in Figs. 12(c), (e), (g) and (i) with that in Fig. 12(a) shows that high-order frequencies are important characteristics in identifying the cracked rotors. However, their amplitudes are weak at several imbalance orientation angles. These high-order frequency components with weak amplitudes cannot be effectively rec-
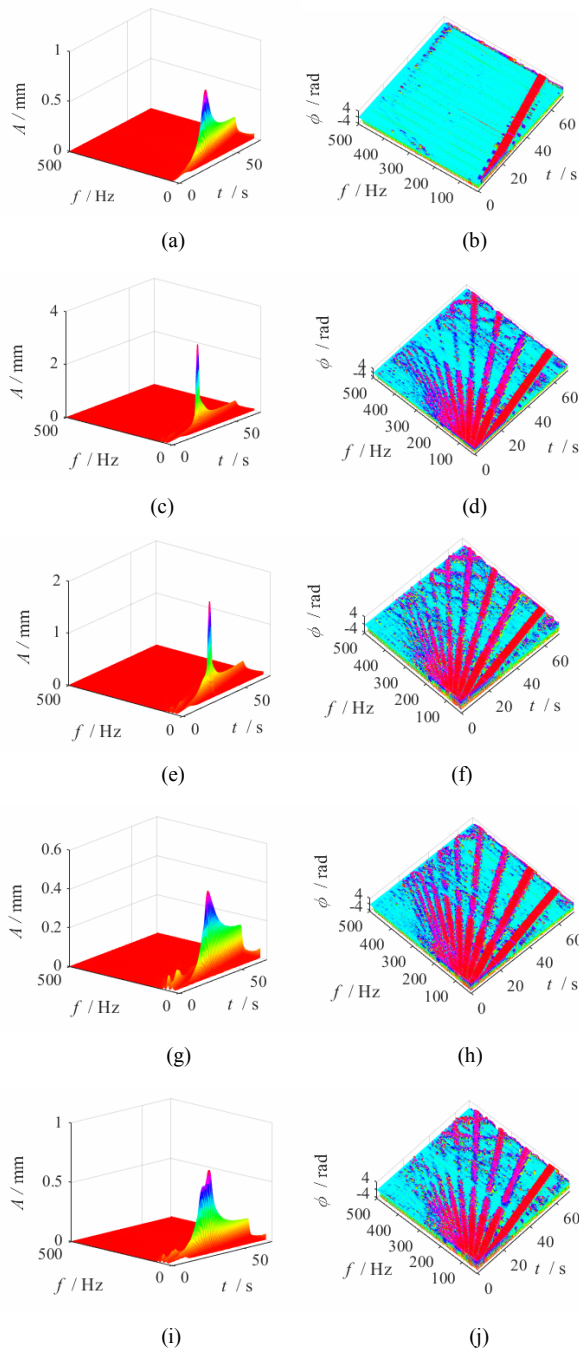
Fig. 12. Dynamic response characteristics of cracked rotors passing through the critical speed at $\mu = 0.2$, $\omega_0 = 1000$ r / min, $\gamma = 9$ rad / s² : (a), (c), (e), (g), (i) Time-frequency amplitude spectrums; (b), (d), (f), (h), (j) phase waterfall plots; (a) and (b) normal rotor; (c) and (d) $\beta = 0$; (e) and (f) $\beta = \pi/2$; (g) and (h) $\beta = \pi$; (i) and (j) $\beta = 3\pi/2$.

ognized in amplitude spectrums. At the same crack depth, imbalance orientation angles considerably affect the shapes and components of amplitude spectrums. Thus, the use of amplitude spectrums is not a robust method of extracting the characteristic frequencies of cracked rotors.

(2) Compared with the phase waterfall plot in Fig. 12(b), those in Figs. 12(d), (f), (h) and (j) all have remarkable radial

Table 1. Parameters of the experiment.

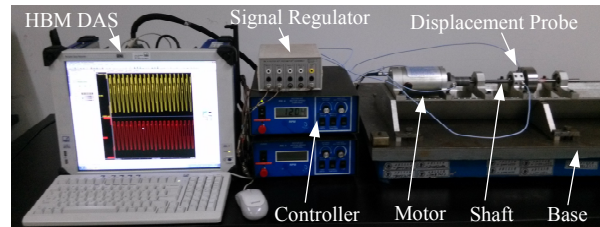| Testing parameters	Values and units
Sampling frequency	3200 (Hz)
Diameter of the disc	80 (mm)
Thickness of the disc	25 (mm)
Critical speed of the test bed	4000 (r/min)
Angular acceleration	9 (rad / s²)

Fig. 13. Bently RK4 rotor test bed and HBM genesis high-speed DAS.

features, which represent the high-order frequency components of the vibration responses of the cracked rotors. These radial features are not influenced by imbalance orientation angles. These high-order frequency components of cracked rotors can hardly be identified in the amplitude spectrums in Figs. 12(c), (e), (g) and (i). Therefore, the radial feature in the phase waterfall plots is an evident characteristic of cracked rotors.

According to the comparative analysis of the characteristics of amplitude spectrum and phase waterfall plots with different imbalance orientation angles, phase waterfall plots are more effective than amplitude spectrums in recognizing weak characteristic frequencies of cracked rotors. Amplitude spectrums can show certain features, but the radial line feature in phase waterfall plots is an evident characteristic of cracked rotors.

4. Experimental study for transient responses

4.1 Introduction of experiment

Experiments are conducted on a Bently RK4 rotor test bed, which is shown in Fig. 3 together with the tested cracked rotor. The rotor test rig mainly includes a speed controller, motor, shaft, and base. The data acquisition system includes a displacement probe, signal regulator, and HBM data acquisition system (DAS). The controller supplies power to the motor and controls the speed of the motor. The displacement probe collects the lateral vibration signal of the shaft and is connected to the HBM DAS through the signal regulator.

The diameter of the steel rotor is 10 mm, and the rotor is supported by two sliding bearings with 225 mm distances. The left end of the rotor is coupled with a drive motor according to a flexible coupling. A crack with approximately 2 mm depth (This crack is a small slot cut by a line-cutting machine. A real crack is then obtained according to a fatigue experiment by a three-point bending fatigue experiment machine.) is present in
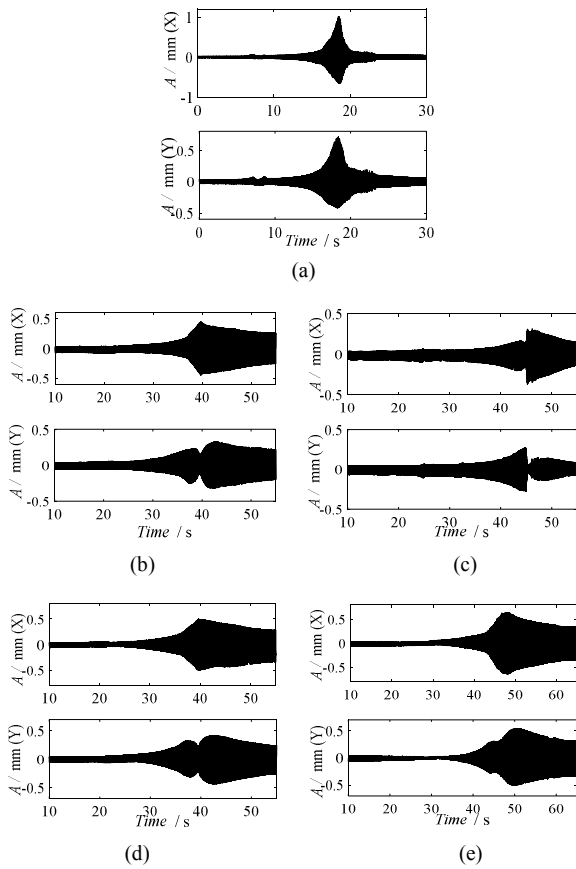
Fig. 14. Time-domain waveforms of the cracked rotor passing through the critical speed: (X) vibration amplitude in X direction, (Y) vibration amplitude in Y direction; (a) normal rotor; (b) $\beta = 0$; (c) $\beta = \pi/2$; (d) $\beta = \pi$; (e) $\beta = 3\pi/2$.

the middle of the rotor. The rotor is generally similar to a Jeff-cott rotor.

The disc of the rotor has 16 thread holes that are evenly positioned to fix the additional eccentric mass, and two eddy current displacement sensors close to the disc are installed on the rotor test bed in the X and Y directions to measure the vibration displacements. The data are collected by HBM genesis high-speed DAS, and the detailed parameters of the testing system are shown in Table 1.

Before the experiment, the dynamic balance operation is adopted to prevent the interference of the inherent imbalance. Then, the additional eccentric mass is added in the corresponding thread hole in the disc to simulate the imbalance in the particular imbalance orientation angle.

The imbalance orientation angles are obtained by the position of the thread hole. In addition, the imbalance orientation angle β is changed four times as follows: $\beta = 0$, $\beta = \pi/2$, $\beta = \pi$ and $\beta = 3\pi/2$. The rotation speed is initially 1000 r/min and then increased to 6500 r/min at a constant acceleration rate.

4.2 Time-domain waveforms

Fig. 14(a) shows the time-domain waveforms of a normal

rotor, and Figs. 14(b)-(e) show the waveforms corresponding to the imbalance orientation angles $\beta = 0$, $\beta = \pi/2$, $\beta = \pi$ and $\beta = 3\pi/2$.

Comparing with the numerical case study in Sec. 3.2, the features of the time-domain waveforms from the simulation data and those from the experimental data are remarkably similar. The waveforms in Figs. 8(a) and 14(a) both have a single resonance peak, which is a feature of a normal rotor. The waveforms in Figs. 8(d) and (e) and those in Figs. 14(d) and (e), respectively, agree well. The vibration waveforms have noticeable double resonance peaks in the Y direction. Although the waveforms in Figs. 8(c) and 14(c) are slightly different, both of them have sharp double resonance peaks. The waveforms in Figs. 8(b) and 14(b) in the Y direction both have double resonance peaks.

This comparative analysis shows that the time-domain waveforms of the numerical and experimental studies agree. Therefore, the effectiveness of the adopted model for major vibration feature extraction can be validated. The breathing stiffness is the intermediate variable of the dynamic model, and it is closely related to the response of the dynamic model. Although we cannot obtain the breathing stiffness in the experiment to justify this breathing mechanism model directly, the good agreement of the vibration response can justify this breathing mechanism model indirectly.

4.3 Phase waterfall plots and time–frequency amplitude spectrums

Figs. 15(a) and (b) are the time–frequency amplitude spectrum and phase waterfall plots of a normal rotor. Figs. 15(c)-(j) correspond to the four time–frequency amplitude spectrums and phase waterfall plots of the cracked rotors at imbalance orientation angles $\beta = 0$, $\beta = \pi/2$, $\beta = \pi$ and $\beta = 3\pi/2$, respectively.

Figs. 15(a) and (b) show that only one frequency component in the spectrum corresponds to the rotational speed. As this speed increases, the radial feature in the phase waterfall plot becomes decreasingly remarkable for the normal rotor.

When the rotor is cracked, the dynamic response characteristics change noticeably. Figs. 15(c)-(j) show the following.

(1) Once a crack appears, all the phase waterfall plots show noticeable radial features and the amplitude of the high-order frequencies are weakened. These features are not influenced by imbalance orientation angles. Therefore, the radial features in phase waterfall plots are the typical features of cracked rotors.

(2) The high-order frequencies in amplitude spectrums are the characteristic frequencies of cracks, but their amplitudes are not significant. Therefore, recognizing cracks is difficult. Furthermore, the features in amplitude spectrums are influenced by imbalance orientation angles. Thus, the features in phase waterfall plots are more robust than those in amplitude spectrums.

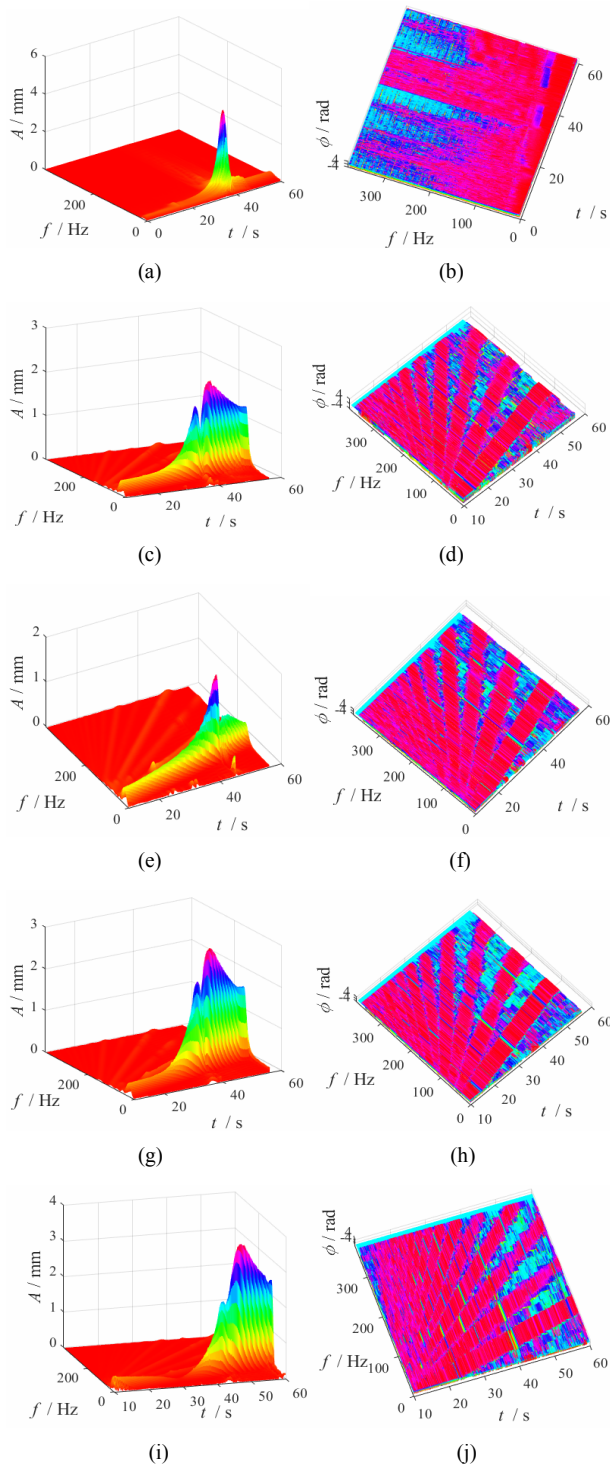Compared with the numerical case study results shown in

(a)

(b)

(c)

(d)

(e)

(f)

(g)

(h)

(i)

(j)

Fig. 15. Dynamic response characteristics of cracked rotors passing through the critical speed at $\gamma = 9 \ \text{rad}/\text{s}^2$: (a), (c), (e), (g) and (i) Time-frequency amplitude spectrums; (b), (d), (f), (h) and (j) phase waterfall plots; (a) and (b) normal rotor; (c) and (d) $\beta = 0$; (e) and (f) $\beta = \pi/2$; (g) and (h) $\beta = \pi$; (i) and (j) $\beta = 3\pi/2$.

Fig. 12 in Sec. 3.4, the dynamic response characteristics of the simulation data agree well with those of the experimental data. The amplitude spectrums in Figs. 12 and 15 mainly contain

fundamental frequency components, and the amplitudes of high-order frequency components are remarkably small. Furthermore, the major features of the phase waterfall plots in Figs. 12 and 15 are noticeably close and both have evident radial features.

Therefore, the effectiveness of the proposed model for the major vibration feature extraction of cracked rotors is further validated. Phase waterfall plots are an effective means of recognizing weak characteristic frequencies of cracked rotors, and the radial feature in these plots is an evident characteristic of cracked rotors.

5. Conclusions

This work proposes an algorithm for calculating the stiffness breathing functions of cracked Jeffcott rotors without weight dominance on the basis of bending theory. A model for cracked rotor systems is also constructed. The vibration features of cracked rotors passing through the critical speed are studied through numerical cases and experiments. A novel phase waterfall plot method that can identify frequency components with weak amplitudes is proposed for the analysis of the vibration response characteristics of cracked Jeffcott rotors. The major conclusions are as follows.

(1) The restoring force modified model proposed in this work adds the iterative process for the solution of the restoring force. The restoring force of the cracked rotor in the whirling process can be solved using this method instead of the hypothesis that the direction of the restoring force is parallel to the shaft displacement. Therefore, the proposed model satisfies the condition without weight dominance.

(2) A novel phase waterfall plot method that can identify frequency components with weak amplitudes is proposed. Features of the phase waterfall plots and time–frequency amplitude spectrums at different imbalance orientation angles are compared. Results show that the phase waterfall plot is an effective and robust means of detecting the high-order frequency components of cracked rotors. The radial feature in phase waterfall plots is an evident characteristic of cracked rotors, which can provide references for crack monitoring.

(3) The time-domain waveforms of vibration displacement signals at different imbalance orientation angles during the passing through the critical speed are comparatively studied. Double resonance peak characteristics in the simulation signals and experimental data agree well, thereby potentially validating the effectiveness of the proposed model for cracked rotors.

Nomenclature————————————

oxy	: Fixed coordinate system
$o'x'y'$	: Rotating coordinate system
$\overrightarrow{o'N}$	: Normal direction of the crack tip
H	: Horizontal reference axis
θ	: Rotation angle
φ	: Whirling angle
ψ	: Rotation–whirling difference angle
d	: Absolute depth of the cracks
μ	: Relative depth of the cracks
D	: Diameter of the shaft
①	: Uncracked area
②	: Closed crack area
③	: Open crack area
o_I	: Centroid
x_I, y_I	: Centroid principal inertia axes
$o_I x^* y^*$	: Coordinate system
$\eta\ (\eta_0)$	: Angle between x_I and x^*
$\boldsymbol{F}_i$	: Restoring force
$\overrightarrow{oo'}$	: Shaft displacement
$\alpha_i\ (\alpha_0)$	: Angle between $\boldsymbol{F}_i$ and $\overrightarrow{oo'}$
$I_{x^*}, I_{y^*}, I_{x^*y^*}$	: Inertia moment of the closed area
$k_{x^*}, k_{y^*}, k_{x^*y^*}$	: Stiffnesses with respect to the $o_I x^* y^*$ coordinate
k_x, k_y, k_{xy}	: Stiffnesses with respect to the oxy coordinate
K_{max}	: Stiffness of the normal shaft
L	: Length of the shaft
z_c	: z-coordinate of the crack position
F_{xI}, F_{yI}	: Component forces of $\boldsymbol{F}_i$
I_x, I_y	: Principal inertia moments
x_i, y_i	: Centroid coordinates of the ith area element
A_i	: Area of the ith area element
E	: Young's modulus
o_c	: Center of mass
e	: Eccentricity
β	: Imbalance orientation angle
$\mathbf{M}$	: Mass matrix
$\mathbf{C}$	: Damping matrix
$\mathbf{K}$	: Stiffness matrix
$\mathbf{F}_s$	: Dead weight
$\mathbf{F}_e$	: External force caused
$\boldsymbol{u}, \dot{\boldsymbol{u}}, \ddot{\boldsymbol{u}}$	: State variable
m	: Mass
γ	: Angular acceleration
ω_0	: Initial angular velocity
$y_i(t)$	: Short-time signals
φ_i	: Initial phases of $y_i(t)$
$Y_i(\omega)$	: Frequency spectrums of $y_i(t)$
$\Phi_i(\omega)$	: Phase spectrums of $y_i(t)$

References

[1] I. W. Mayes and W. G. R. Davies, Analysis of the response of a multi-rotor-bearing system containing a transverse crack in a rotor, *Journal of Vibration, Acoustics, Stress, and Reliability in Design*, 106 (1) (1984) 139-145.

[2] A. S. Sekhar and B. S. Prabhu, Condition monitoring of cracked rotors through transient response, *Mechanism and Machine Theory*, 33 (8) (1998) 1167-1175.

[3] J. J. Sinou and A. W. Lees, The influence of cracks in rotating shafts, *Journal of Sound and Vibration*, 285 (4) (2005) 1015-1037.

[4] J. J. Sinou and A. W. Lee, A non-linear study of a cracked rotor, *European Journal of Mechanics-A/Solids*, 26 (1) (2007) 152-170.

[5] J. T. Sawicki, A. L. Gyekenyesi and G. Y. Baaklini, Analysis of transient response of cracked flexible rotor, *Conference on Nondestructive Evaluation and Health Monitoring of Aerospace Materials and Composites III*, San Diego, CA (2004) 142-150.

[6] M. A. Al-Shudeifat and E. A. Butcher, New breathing functions for the transverse breathing crack of the cracked rotor system: approach for critical and subcritical harmonic analysis, *Journal of Sound and Vibration*, 330 (3) (2011) 526-544.

[7] C. Guo, M. A. Al-Shudeifat and J. Yan, Stability analysis for transverse breathing cracks in rotor systems, *European Journal of Mechanics-A/Solids*, 42 (2013) 27-34.

[8] C. Guo, M. A. Al-Shudeifat and J. Yan, Application of empirical mode decomposition to a Jeffcott rotor with a breathing crack, *Journal of Sound and Vibration*, 332 (16) (2013) 3881-3892.

[9] N. Bachschmid, P. Pennacchi and E. Tanzi, Transverse crack modeling and validation in rotor systems, including thermal effects, *International Journal of Rotating Machinery*, 9 (2) (2003) 113-126.

[10] N. Bachschmid, P. Pennacchi and E. Tanzi, *Cracked rotors: A survey on static and dynamic behaviour including modelling and diagnosis*, Springer-Verlag, Berlin, Heidelberg, Germany (2010).

[11] L. Cheng, N. Li and X. F. Chen, The influence of crack breathing and imbalance orientation angle on the characteristics of the critical speed of a cracked rotor, *Journal of Sound and Vibration*, 330 (9) (2011) 2031-2048.

[12] P. Pennacchi, N. Bachschmid and A. Vania, A model-based identification method of transverse cracks in rotating shafts suitable for industrial machines, *Mechanical Systems and Signal Processing*, 20 (8) (2006) 2112-2147.

[13] T. R. Babu and A. S. Sekhar, Detection of two cracks in a rotor-bearing system using amplitude deviation curve, *Journal of Sound and Vibration*, 314 (3) (2008) 457-464.

[14] T. R. Babu, S. Srikanth and A. S. Sekhar, Hilbert–Huang transform for detection and monitoring of crack in a transient rotor, *Mechanical Systems and Signal Processing*, 22 (4) (2008) 905-914.

[15] A. S. Sekhar, Multiple cracks effects and identification, *Mechanical Systems and Signal Processing*, 22 (4) (2008) 845-878.

[16] K. Saravanan and A. S. Sekhar, Vibration based statistical features for shaft crack detection in a rotor, *Advances in Vibration Engineering*, 12 (5) (2013) 447-458.

[17] G. M. Dong and J. Chen, Crack identification in a rotor with an open crack, *Journal of Mechanical Science and Technology*, 23 (11) (2009) 2964-2972.

[18] J. P. Spagnol, H. Wu and K. Xiao, Dynamic response of a cracked rotor with an unbalance influenced breathing mechanism, *Journal of Mechanical Science and Technology*, 32 (1) (2018) 57-68.

[19] J. Zhao, H. DeSmidf and W. Yao, Coupled vibration of nonlinear breathing cracked rotor in lateral, torsional and longitudinal DOFs, *Conference on Health Monitoring of Structural and Biological Systems*, San Diego, CA (2015) 94380F-94380F-9.

[20] X. B. Rao, Y. D. Chu and Y. X. Chang, Dynamics of a cracked rotor system with oil-film force in parameter space, *Nonlinear Dynamics*, 88 (4) (2017) 2347-2357.

[21] H. Khorrami, S. Rakheja and R. Sedaghati, Vibration behavior of a two-crack shaft in a rotor disc-bearing system, *Mechanism and Machine Theory*, 113 (2017) 67-84.

[22] C. Liu and D. Jiang, Dynamics of slant cracked rotor for a steam turbine generator system, *Journal of Engineering for Gas Turbines and Power*, 139 (6) (2017) 062502-062502-7.

[23] N. H. Chandra and A. S. Sekhar, Fault detection in rotor bearing systems using time frequency techniques, *Mechanical Systems and Signal Processing*, 72 (2016) 105-133.

[24] Z. Hu, J. Tang and J. Zhong, Frequency spectrum and vibration analysis of high speed gear-rotor system with tooth root crack considering transmission error excitation, *Engineering Failure Analysis*, 60 (2016) 405-441.

[25] C. Guo, J. Yan and W. Yang, Crack detection for a Jeffcott rotor with a transverse crack: An experimental investigation, *Mechanical Systems and Signal Processing*, 83 (2017) 260-271.

[26] S. Singh and N. Kumar, Combined rotor fault diagnosis in rotating machinery using empirical mode decomposition, *Journal of Mechanical Science and Technology*, 28 (12) (2014) 4869-4876.

Appendix

A. Detailed processes of the restoring force modified model

(1) The cross section is divided into many area elements, as shown in Fig. 1. At each rotation–whirling difference angle ($\psi = \psi + i\Delta\psi$), the following iterative calculations are performed on the discrete section to solve the open and closed area of the cracked section, the position of the centroid principal inertia axes (η), and the principal inertia moments (I_x, I_y) with respect to the principal inertia axes (x_I, y_I).

(2) The angle of the restoring force is assumed to be $\alpha_0 = -\pi$, as shown in Fig. 2(a).

(3) The centroid o_I is assumed to coincide with the origin o' and the centroid principal inertia axes (x_I, y_I) with the rotating coordinate axes ($\eta_0 = 0$), as shown in Fig. 2(a).

(4) According to the theory of material mechanics and by ignoring the stress concentration, the stress of the *i*th area element can be calculated by Eq. (A.1).

$$\sigma_i = \frac{-F_{x_I}(L - z_c)z_c}{LI_y}y_i + \frac{-F_{y_I}(L - z_c)z_c}{LI_x}x_i, \tag{A.1}$$

where L is the length of the shaft, z_c is the z-coordinate of the crack position with respect to the *o-xyz* reference system (in this study, $z_c = L/2$.), as shown in Fig. 6. F_{xI} and F_{yI} are the component forces of F_i in the x_I and y_I directions, I_x and I_y are the principal inertia moments corresponding to the centroid principal inertia axes x_I and y_I, respectively, as shown in Fig. 2. x_i and y_i are the centroid coordinates of the *i*th area element with respect to the $o_Ix_Iy_I$ reference system.

The sign of the stress can be checked at each area element of the cracked area. A plus sign means tension. No contact force is present at this point (the cracked area element is opening; area ③). A minus sign means compression. Contact forces are present (the cracked area element is closed; area ②).

(5) Total closed areas ①+② are determined. According to the theory of material mechanics, the new centroid of the total closed area can be calculated by Eq. (A.2).

$$x_{o_I} = \frac{\sum_{i=1}^{n} x_i A_i}{\sum_{i=1}^{n} A_i} \qquad y_{o_I} = \frac{\sum_{i=1}^{n} y_i A_i}{\sum_{i=1}^{n} A_i}, \tag{A.2}$$

where A_i is the area of the *i*th discrete area element, x_{oI} and y_{oI} are the coordinates of the centroid o_I with respect to the $o'x'y'$ reference system, and x_i and y_i are the centroid coordinates of the *i*th area element for the same reference system.

The angle η can be calculated with the axial conversion Eq. (A.3).

$$\tan(2\eta) = -\frac{2I_{x^*y^*}}{I_{y^*} - I_{x^*}}, \tag{A.3}$$

where I_{x^*}, I_{y^*} and $I_{x^*y^*}$ represent the inertial moments and inertial product with respect to x^* and y^* axes, which can be calculated by Eq. (A.4).

$$I_{x^*} = \sum_{i=1}^{n} y_i^2 A_i \quad I_{y^*} = \sum_{i=1}^{n} x_i^2 A_i \quad I_{x^*y^*} = \sum_{i=1}^{n} x_i y_i A_i, \tag{A.4}$$

where x_i and y_i are the centroid coordinates of the *i*th area element with respect to the $o_I x^* y^*$ reference system.

(6) Steps (3)-(5) are repeated with the updated o_I and η until η converges into a stable value, as shown in Figs. 2(b) and 3.

(7) To simplify the model and investigate the main mechanical characteristics in the Jeffcott rotor model, the z-axis DOF is not considered. Thus, in this breathing mechanism model, we assume the open part in crack section to be throughout the shaft.

This procedure can substantially simplify the calculations of

stiffness and restoring force and can extract the main change law of breathing stiffness. This simplified model satisfies the requirements of qualitative vibration characteristic analysis and mechanism explanations of cracked rotors, although part of the accuracy of vibration amplitude may be lost. All models have limitations, and no absolute best model exists. Therefore, the most appropriate model should be established according to the analysis requirements.

When high accuracy of vibration amplitude is needed, the entire shaft should be divided into a local cracked shaft and two normal shafts, which connect with the local cracked shaft by both ends.

The inertial moments and products I_{x*}, I_{y*} and I_{x*y*} are known. On the basis of the above simplification and the theory of material mechanics, the stiffnesses k_{x*}, k_{y*} and k_{x*y*} can then be calculated by Eq. (A.5), where E is Young's modulus.

$$k_* = \frac{48EI_*}{z_c(3L^2 - 4z_c^2)}. \tag{A.5}$$

The stiffnesses k_x, k_y and k_{xy} with respect to the x and y axes can then be calculated by axial conversion (Eq. (A.6)).

$$\begin{bmatrix} k_x \\ k_y \\ k_{xy} \end{bmatrix} = \begin{bmatrix} \cos^2(\varphi) & \sin^2(\varphi) & -\sin(2\varphi) \\ \sin^2(\varphi) & \cos^2(\varphi) & \sin(2\varphi) \\ \sin(\varphi)\cos(\varphi) & -\sin(\varphi)\cos(\varphi) & \cos(2\varphi) \end{bmatrix} \bullet \begin{bmatrix} k_{x'} \\ k_{y'} \\ k_{x'y'} \end{bmatrix}, \tag{A.6}$$

where φ is the whirling angle of the axis in the fixed coordinate.

(8) The restoring force $\boldsymbol{F}_i$ and the angle α_i can be calculated by Eqs. (A.7) and (A.8).

$$\boldsymbol{F}_i = -\begin{bmatrix} k_x & k_{xy} \\ k_{xy} & k_y \end{bmatrix} \begin{bmatrix} x_{o'} \\ y_{o'} \end{bmatrix}, \tag{A.7}$$

$$\cos\alpha_i = \frac{\boldsymbol{F}_i \overrightarrow{oo'}}{|\boldsymbol{F}_i||\overrightarrow{oo'}|}, \tag{A.8}$$

where $x_{o'}$ and $y_{o'}$ are the relative displacements of centroid o' with respect to the *oxy* reference coordinate.

Steps (2)-(8) are repeated with the updated $\boldsymbol{F}_i$ and α_i until α_i converges into a stable value, as shown in Figs. 2(c), (d) and 3.

(9) The stiffness $K^*(\psi) = [k_{x*}, k_{y*}, k_{x*y*}]$ is saved at the present rotation–whirling difference angle ψ.

(10) The turn–whirling difference angle $\psi = \psi + \Delta\psi$ is updated, and Steps (2)-(9) are repeated. Then, the stiffness $K^*(\psi) = [k_{x*}, k_{y*}, k_{x*y*}]$ at each ψ can be obtained.

Jingsong Xie obtained his B.S. from the School of Mechanical Engineering at Northwestern Polytechnical University in 2013. He is currently studying at Xi'an Jiaotong University for his Ph.D. in engineering. His research interests include rotor dynamics, vibration analysis, and crack diagnosis.

Wei Cheng obtained his B.S., M.S., and Ph.D. from the School of Mechanical Engineering at Xi'an Jiaotong University in 2006, 2008, and 2012, respectively. He is currently an Associate Professor at Xi'an Jiaotong University. His research interests include vibration transfer path analysis, vibration source contribution evaluation, and machinery fault diagnosis.

Yanyang Zi obtained his B.S. and Ph.D. from the School of Mechanical Engineering at Xi'an Jiaotong University in 1993 and 2001, respectively. He is currently a Professor at the Department of Mechanical Engineering in Xi'an Jiaotong University. His research interests include vibration signal processing, machinery condition monitoring, and fault diagnosis.